

A compact symmetric ejection from the low mass AGN in the LINER galaxy NGC 4293

Xiaolong Yang,^{1,2*} Ruiling Wang,³ Quan Guo¹

¹Shanghai Astronomical Observatory, Key Laboratory of Radio Astronomy, Chinese Academy of Sciences, Shanghai 200030, China

²Shanghai Key Laboratory of Space Navigation and Positioning Techniques, Shanghai Astronomical Observatory, Chinese Academy of Sciences, Shanghai 200030, China

³Astronomical Research Station of Shanghai Astronomical Observatory, Chinese Academy of Sciences, Shanghai 200030, China

Accepted XXX. Received YYY; in original form ZZZ

ABSTRACT

We conducted a Very Long Baseline Array (VLBA) observation of the low mass active galactic nucleus (AGN) in galaxy NGC 4293 ($z = 0.003$). The object is associated with a low-ionization nuclear emission-line region (LINER). Its black hole mass is estimated as $\sim 10^5$ or $\sim 10^7 M_\odot$. The VLBA 1.5 GHz image shows an inverse symmetric structure with two discrete radio blobs separated by an angular distance of ~ 120 mas, corresponding to ~ 7 parsec. Furthermore, its integrated radio spectrum has a turnover at the frequency of ~ 0.44 GHz. Based on the compactness and spectrum, the nuclear radio source in NGC 4293 belongs to a sample of (megahertz) peaked spectrum (PS/MPS) radio sources with compact symmetric morphologies. NGC 4293 has 1.4 GHz radio power of only $\sim 10^{20}$ W Hz⁻¹ with the VLBA observation, which is consistent with local AGNs but lower than the current PS samples. One of the two blobs has a steep radio spectrum $\alpha = -0.62 \pm 0.08$ ($S_\nu \propto \nu^{+\alpha}$), while the other one has an inverted spectrum $\alpha = 0.32 \pm 0.10$. The VLBA 1.5 GHz luminosity ratio of the two blobs is 3.23 and both blobs show lateral-flowing structures where the hotspots reside at the edge of each radio lobe. This can be explained as jet interactions with dense circumnuclear medium. We estimate the black hole mass of NGC 4293 through the fundamental plane of black hole activity, which constrains the black hole mass to be $\lesssim 10^6 M_\odot$. It supports that the object is a low-mass AGN and a potential candidate for accreting and ejecting IMBHs.

Key words: galaxies: active – galaxies: individual: NGC 4293 – radio continuum: galaxies – galaxies: jets

1 INTRODUCTION

Stellar-mass black holes (SBHs), formed from the direct collapses of massive stars (Mirabel 2017), are widely observed in the Universe. Supermassive black holes (SMBHs, $10^6 - 10^{10} M_\odot$) are also universally found in the centers of galaxies with bulges (Kormendy & Ho 2013). However, the gap between two classes of black holes, i.e. the so-called intermediate-mass black holes (IMBHs, $10^2 - 10^6 M_\odot$, see review by Greene et al. 2020), remains unfilled (especially $10^3 - 10^4 M_\odot$). The necessity for the existence of IMBHs is strongly suggested by SMBHs with masses up to $10^{10} M_\odot$ (Wu et al. 2015; Bañados et al. 2018) in the early Universe, when the Universe was only 5% of its current age. These discoveries pose challenges to the formation of SMBHs, and intermediate-mass (seed) black holes are required to form SMBHs at such an early age.

Based on the expected formation and evolution scenarios, observational searches for IMBHs have typically focused on the following habitats: globular clusters, ultra/hyper-luminous X-ray sources, and dwarf galaxies, there is growing evidence for the abundance of $10^5 M_\odot$ IMBHs in dwarf galaxies with stellar masses ranging from $10^7 - 10^{10} M_\odot$ (e.g. Greene & Ho 2004, 2007; Dong et al. 2012; Reines et al. 2013; Liu et al. 2018; Chilingarian et al. 2018; Mezcua et al. 2018). Moreover, black holes with $10^4 - 10^6$ solar masses dis-

covered in the centers of nearby dwarf galaxies are thought to be formed in the early Universe (Volonteri 2010; Greene 2012). These dwarf galaxies have undergone few merger events in their evolutionary history and therefore have not grown significantly since their birth. Thus, the central black holes in dwarf galaxies still retain the footprints of the seed black holes, providing valuable clues for our study of the formation and evolution of SMBHs in the early Universe (Volonteri 2010; Inayoshi et al. 2020).

Radio jets/outflows are the fundamental parts of both SBHs and SMBHs which maintain accretion process (e.g. Faucher-Giguère & Quataert 2012; King & Pounds 2015). Continuum imaging and spectral studies can be used to infer the observational signatures of mildly relativistic to relativistic outflows ($0.1 - 1.0 c$ respectively, e.g. Nyland et al. 2017; Saikia et al. 2018; Hwang et al. 2018; Yang et al. 2021) and hence, the activity of IMBHs that are hosted in Active Galactic Nuclei (AGNs). A pilot radio survey and study of low-mass AGNs with high accretion rates by Greene et al. (2006) indicates that these sources are predominantly radio-quiet. These signatures may be explained by comparison with Galactic X-ray binaries (hosting stellar mass black holes) where the high/soft X-ray state is characterized by a quenched radio emission (e.g. McClintock & Remillard 2006). It is generally believed that the accretion process in SMBHs and SBHs are similar and scale independent (e.g. Svoboda et al. 2017). Simultaneously, the high/soft state in Galactic X-ray binaries is radio quiet, while the transition from a low/hard state to a high/soft

* E-mail: yangxl@shao.ac.cn

state is often associated with transient jets/outflows. On studying of a sample of high accretion rate IMBHs show that the ejection process in IMBHs is likely episodic, and in some cases the radio core is visible and in other cases, it is not (Yang et al. 2022, In preparation). A recent study of the IMBH candidate NGC 4395 reveals both fossil radio ejecta and diffuse and flat-spectrum radio emission in the nucleus (Yang et al. 2022), and a thermal mechanism in the nucleus is proposed correspondingly.

Very Long Baseline Interferometry (VLBI) observations offer high angular resolutions (at the milli-arcsec scale) in radio band, surpassing other imaging techniques in astronomy. The VLBI detection of compact pc-scale radio-emitting structures (core/core-jet/jet-knot) in the nuclear regions of dwarf galaxies can directly probe the jet/outflow activity enabled by an accreting, potential IMBH. To date, high-resolution VLBI observational studies are limited to only a few IMBH candidate hosts: NGC 4395 (Wrobel & Ho 2006; Yang et al. 2022), Henize 2-10 (Reines & Deller 2012), NGC 404 (Paragi et al. 2014) and RGG 9 (Yang et al. 2020a). In order to understand the ejection process in actively accreting IMBHs, we present an observational study of an IMBH candidate in NGC 4293.

NGC 4293, at redshift $z = 0.003$, was identified as a late-type spiral galaxy with a low-ionization nuclear emission-line region (LINER, Ho et al. 1997a; Decarli et al. 2007). The black hole mass of its AGN was estimated as $\log(M_{\text{BH}}/M_{\odot}) = 7.7$ through the black hole mass (M_{BH}) and velocity dispersion (σ) relation (Chiba et al. 2005). Another work obtained a similar black hole mass $\log(M_{\text{BH}}/M_{\odot}) = 7.5$ by taking the black hole mass - K_s -band bulge luminosity relation (Dong & De Robertis 2006). Recently, Chilingarian et al. (2018) used the single-epoch broad H α emission to measure the black hole mass of NGC 4293. This source was re-weighted as $\log(M_{\text{BH}}/M_{\odot}) = 5.30 \pm 0.06$, and hence an IMBH candidate. Nagar et al. (2002, 2005) observed NGC 4293 at 15 GHz with Very Large Array (VLA) A-array, they obtained a resolution of 0.15 arcsec and yielded a integrated flux density of ~ 1.4 mJy (with merely a signal-to-noise ratio of ~ 5). With the VLA A-array 15 GHz observation and VLA archive data at 1.5 and 5 GHz, Nagar et al. (2002) measured a steep radio spectrum ($\alpha < -0.3$ according to their definition and $S \propto \nu^{+\alpha}$, while in this work, a spectrum is termed as steep, flat or inverted when $\alpha \leq -0.5$, $-0.5 < \alpha < 0$ or $\alpha > 0$, respectively) in NGC 4293. While comparing with the 15 GHz observation and a Multi-Element Radio Linked Interferometer Network (MERLIN) 5 GHz observation, Filho et al. (2006) conclude a flat radio spectrum. In order to investigate the nuclear (parsec and sub-parsec scale) outflows of NGC 4293, in this work, we report the Very Long Baseline Array (VLBA) observation of the nuclear region in NGC 4293 and we also analyse the archival data from VLA and MERLIN. This paper is organised as follows. In Section 2, we describe multi-band observations and data reduction of the target NGC 4293. In Section 3, we present imaging, spectral and model-fitting results of NGC 4293. In Section 4, we discuss the radio identification of NGC 4293, describe the interpretation of the multi-band properties, and estimate black hole mass. Finally, we give our conclusions in Section 5. Throughout this work, we adopt the standard Λ CDM cosmology with $H_0 = 71$ km s $^{-1}$ Mpc $^{-1}$, $\Omega_{\Lambda} = 0.73$, $\Omega_m = 0.27$ and the corresponding physical scale is 0.061 pc mas $^{-1}$ in NGC 4293.

2 OBSERVATION AND DATA REDUCTION

We observed NGC 4293 with eight VLBA antennas from 2021 July 08 to 09 (UT, the project ID: BA146). The antennas at Kitt Peak (KP) and North Liberty (NL) were unavailable due to equipment

failure. The observation was scheduled at L-band (the central frequency is 1.545 GHz, hereinafter using 1.5 GHz for short), with a total observation time of 3 h and a data recording rate of 2 Gbits per second. Phase-reference mode was used and the quasar 1216+179 (R.A. = 12^h18^m46^s.6045, DEC. = +17°38′17″.268) was chosen as the phase-reference calibrator. The observation was scheduled with a dual polarization mode and a total bandwidth of 320 MHz with 1 min on calibrator and 5 min on target in each observing cycle. The correlated data was processed using the Astronomical Image Processing System (AIPS, Greisen 2003) developed by the National Radio Astronomy Observatory (NRAO) of the USA. A prior amplitude calibration was performed using the system temperatures and the antenna gain curves provided by each VLBA station. The Earth orientation parameters were obtained and calibrated using the measurements from the U.S. Naval Observatory database, and the ionospheric dispersive delays were corrected from a map of the total electron content provided by the Crustal Dynamics Data Information System (CDDIS) of NASA¹. The opacity and parallactic angles were also corrected using the auxiliary files attached to the data. A global fringe-fitting on the phase-reference calibrator 1216+179 was performed, taking the calibrator’s model to solve miscellaneous phase delays of the target.

The target source’s data were exported into DIFMAP (Shepherd 1997) for imaging and model-fitting. The final image was created with natural weighting through the task ‘CLEAN’, see Figure 1. We estimate flux density uncertainties following the instructions described by Fomalont (1999). In this work, the integrated flux densities S_i were extracted from Gaussian model-fit in DIFMAP with the task ‘MODELFIT’, where a standard deviation in model-fit was estimated for each component and considered as the fitting noise error. Additionally, we assign the standard 5% errors originating from amplitude calibration of VLBA (see VLBA Observational Status Summary 2021A²). The final image gives a $1 - \sigma$ rms noise of 0.03 mJy beam $^{-1}$ and a beam size of 13×4.52 mas at a position angle of -8.58° .

Furthermore, we also retrieved MERLIN data from MERLIN archive³ and VLA data from the NRAO data archive⁴. The MERLIN 5 GHz data was observed on June 12th, 2004 and it is likely the same observation that was published by Filho et al. (2006), the total bandwidth of MERLIN observation is 15 MHz. In this work, we used the reduced data from the MERLIN archive. A manual deconvolution and two-dimensional Gaussian model-fitting were done in DIFMAP with the DIFMAP task ‘CLEAN’ and ‘MODELFIT’, respectively. The final image gives a $1 - \sigma$ rms noise of 0.1 mJy beam $^{-1}$ and a beam size of 79×49 mas at a position angle of 26° . The radio observation at 4.86 GHz and 8.46 GHz were taken from VLA archive project AS0806 (PIs or Observers are Schmitt et al.), which were carried out with a configuration of VLA A-array and a total bandwidth of 50 MHz, on 2004 October 23. We obtained the reduced data from the NRAO archive and performed a manual deconvolution and two-dimensional Gaussian model-fitting in DIFMAP to retrieve the information of a central compact component, the results are shown in Table 1, where the $1 - \sigma$ rms noise is 0.06 and 0.04 mJy beam $^{-1}$, respectively. The flux density uncertainties for MERLIN and VLA

¹ <https://cddis.nasa.gov>

² <https://science.nrao.edu/facilities/vlba/docs/manuals/oss2021A>

³ <http://www.merlin.ac.uk/archive/acknowledge.html>
emerlin.support@j.b.man.ac.uk

⁴ <https://archive.nrao.edu/archive/advquery.jsp>

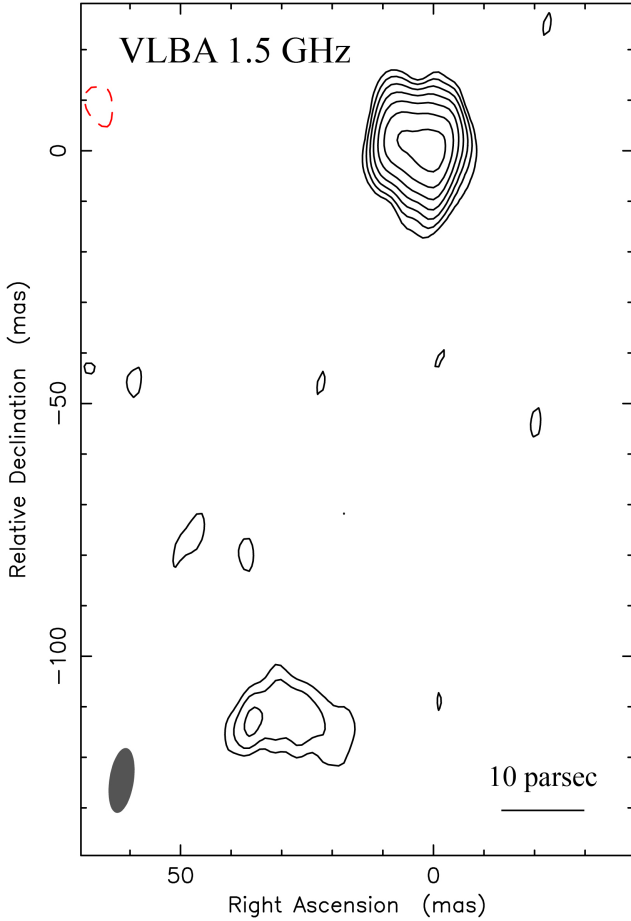


Figure 1. Naturally-weighted VLBA 1.5 GHz image of the core region in NGC 4293. The map reference is at the peak position of radio flux density. The contours are at $3\sigma \times (-1, 1, 1.41, 2, 2.83, \dots)$, here 1σ noise is $0.03 \text{ mJy beam}^{-1}$. The black solid contours represent positive values and the red dashed contours represent negative values. The grey ellipse in the bottom left corner represents the full-width at half-maximum (FWHM) of the restoring beam, which is $13 \times 4.52 \text{ mas}$ at a position angle -8.58° .

data are estimated following the same method described in Yang et al. (2020b).

3 RESULTS

In Figure 1, we show the naturally weighted VLBA L-band (1.5 GHz) image. The source shows a symmetric structure with two discrete lobes, where we mark the North-West component as ‘N’ and the South-East component as ‘S’. The peak flux densities of N and S are 2.70 ± 0.17 and $0.72 \pm 0.05 \text{ mJy beam}^{-1}$, respectively, yielding an SNR of 40 and 10, respectively, indicating clear detections. Both components N and S have counterparts in the MERLIN 5 GHz image, see black contours in panel c of Figure 2. We performed two-dimensional Gaussian model fittings on the VLBA L-band and MERLIN C-band uv-visibilitys. Especially, in order to match the resolution between VLBA L and MERLIN C-band, here we downward the resolution of VLBA L-band data by using an uv-taper. The model-fitting results are listed in Table 2. We take the integrated flux density to measure the non-simultaneous radio spectral indices α be-

tween 1.5 and 5 GHz for components N and S, which are -0.64 ± 0.09 and 0.33 ± 0.09 , respectively.

By evaluating the radio spectrum compiled from the non-simultaneous data, we check the variability of NGC 4293 through observations with the same configurations, i.e. at the same frequencies with identical resolutions. Both the two TGSS and VLASS observations satisfy this purpose (see Table 1). These two TGSS observations were conducted in the frequency of 0.147 GHz and an angular scale of 25 arcsec, which results in no significant variability higher than 35% within 6 years from 2010 to 2016. Again, these two VLASS observations were conducted in the frequency of 3 GHz and the angular scale of ~ 2.6 arcsec. A marginal variability of 8.7% can be inferred with a significance of only 2σ within 2.6 years from 2019 to 2021. Therefore, as a conclusion, no clear variability is detected in NGC 4293. The target is unresolved at a resolution poorer than 1 arcsec (see panels b and c of Figure 2), while combining the high-resolution data with low-resolution ones may still result in the loss of diffuse emission. Figure 3 shows the L (1.4) and S-band (3 GHz) observations at different resolutions, where combining the Arecibo 2.38 and Effelsberg 4.85 GHz data, we measured the 3 GHz flux density in ~ 150 arcsec. The plot implies a positive correlation (possibly a power law) between radio flux densities and collection areas, and it likely hints at a similar trend at different frequencies.

We follow the equation described in e.g. Callingham et al. (2017) to model the entire spectrum of NGC 4293. Additionally, here we assume a power-law distribution of radio flux density along angular size according to the observational hints (see Figure 3).

$$S_\nu = \frac{S_p \theta^{\alpha_{size}}}{(1 - e^{-1})} \times \left(1 - e^{-(\nu/\nu_p)^{\alpha_{thin} - \alpha_{thick}}}\right) \times \left(\frac{\nu}{\nu_p}\right)^{\alpha_{thick}} \quad (1)$$

where S_ν is the flux density at frequency ν and angular size θ , ν_p is the frequency at which the spectrum peaks, S_p is the flux density at the frequency ν_p and an unit angular size (i.e. $\theta=1$ arcsec), α_{thick} and α_{thin} are the spectral indices in the optically thick and optically thin regimes of the spectrum, respectively.

A Markov chain Monte Carlo algorithm is used to fit the spectrum, and only the observations with beam size larger than 2 arcsec are taken in the fitting. In Figure 4, we show the posterior probability distributions of each parameter, and we take 16% and 84% of the distributions as the lower and upper limits, respectively, thus representing 1σ confidence ranges. The fitting yields a peak flux density $S_p = 15.65^{+2.04}_{-1.63} \text{ mJy}$ at frequency $\nu_p = 0.44^{+0.14}_{-0.11} \text{ GHz}$ and the angular size $\theta = 1$ arcsec, with optically thin and thick spectral index $\alpha_{thin} = -0.66^{+0.05}_{-0.06}$ and $\alpha_{thick} = 1.29^{+0.58}_{-0.33}$, respectively. Furthermore, the power-law index of flux density distribution along angular size $\alpha_{size} = 0.14 \pm 0.02$. The spectrum of NGC 4293 is plotted in Figure 5, where the black solid line represents the best fit of equation 1 to the integrated radio spectrum at the typical angular size of 20 arcsec. The thin and thick radio spectral indices are consistent with the typical peaked spectrum radio sources (O’Dea 1998). Furthermore, NGC 4293 is resolved and shows diffuse emission along east-west direction in an angular scale of 1 arcsec (see panel c of Figure 2). It shows that the spectrum of the central compact component in VLA A-array 4.86 and 8.46 GHz aligns the integrated spectrum (optically thin part, see Figure 5), which indicates the core dominance in this scale. Assuming a similar flux density distribution along frequencies and sizes, i.e. equation 1 is still applicable in an angular scale of ~ 0.5 arcsec, the equation gives a flux density of 4.67 ± 1.19 and $3.10 \pm 0.85 \text{ mJy beam}^{-1}$ for VLA A-array 4.86 and 8.46 GHz respectively and this is approximately consistent with the observations.

The brightness and compactness of radio components can be pa-

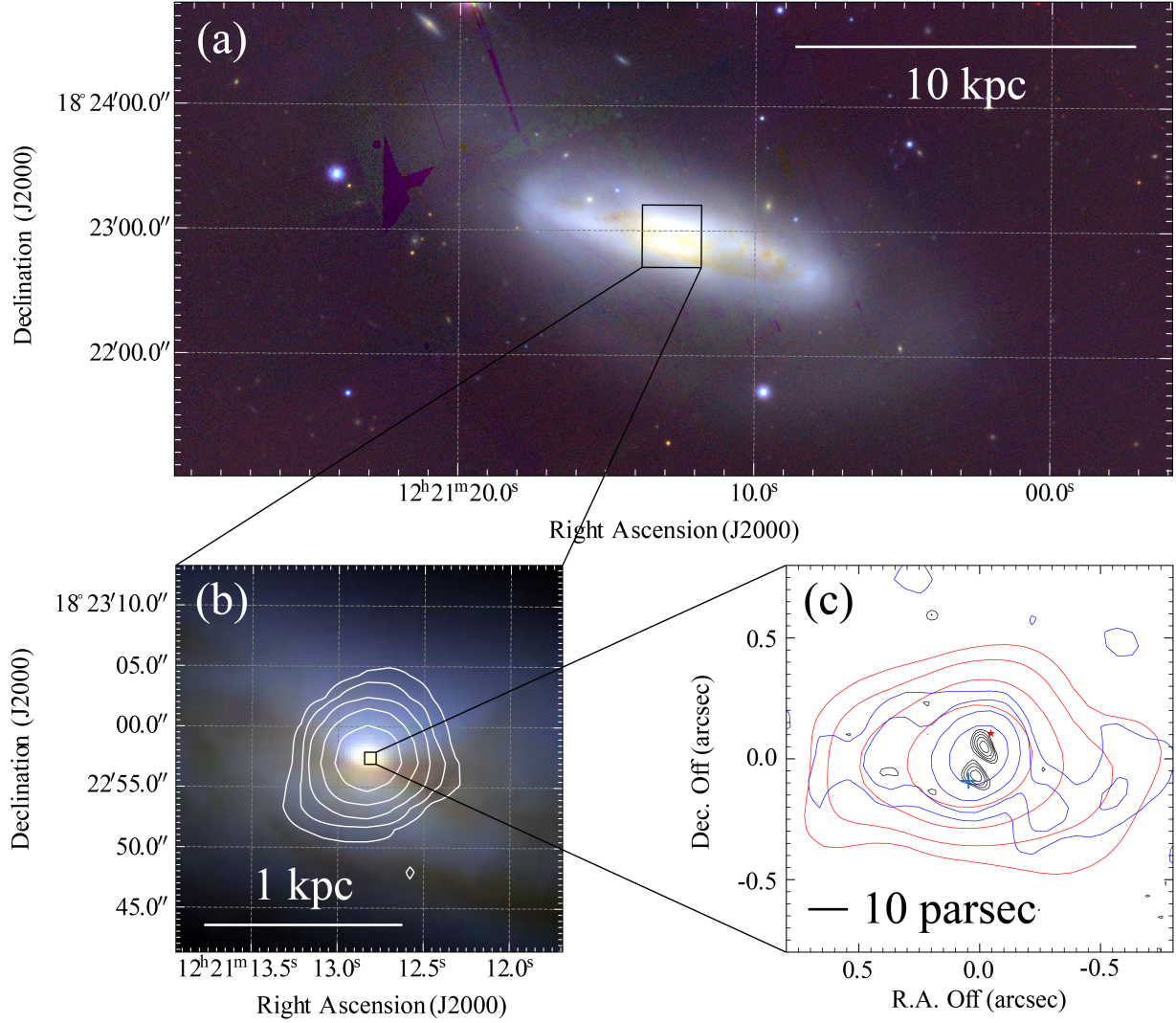


Figure 2. A zooming-in to the central engine of NGC 4293. (a) optical image from Pan-STARRS DR1 (PS1); (b) the FIRST 1.4 GHz contours overlaid on the PS1 color map; (c) radio contours from VLA 4.86 GHz (red), VLA 8.46 GHz (blue) and MERLIN 5 GHz (black) observations, which center on a symmetric center of the VLBA emission in Figure 1, where red star is from *Gaia* early data release 3 (EDR3) and blue cross is from WISE infrared observation. The contours are at $3\sigma \times (-1, 1, 2, 4, 8, \dots)$ for VLA 1.4, 4.86 and 8.46 GHz and $3\sigma \times (-1, 1, 1.41, 2, 2.83, \dots)$ for MERLIN 5 GHz data, here 1σ noise is 0.13, 0.06, 0.04, and 0.1 mJy beam $^{-1}$, respectively.

parameterized by taking the brightness temperatures, measured using the formula (e.g. Ulvestad et al. 2005)

$$T_B = 1.8 \times 10^9 (1+z) \frac{S_i}{\nu^2 \theta^2} \text{ (K)}, \quad (2)$$

where S_i is the integrated flux density of each Gaussian model component in mJy (column 2 of Table 2), θ is FWHM of the Gaussian model in mas (column 4 of Table 2), ν is the observing frequency in GHz, and z is the redshift. The estimated brightness temperatures are listed in column 5 of Table 2. The radio brightness temperatures are inversely proportional to the measured component sizes. Since the measured component sizes are only upper limits, the radio brightness temperatures should be considered as lower limits.

Assuming minimum energy (approximately equipartition) conditions in synchrotron emission, we can estimate the magnetic field

B_{\min} in Gauss (G) through the formula (e.g. Patil et al. 2022)

$$B_{\min} \approx 0.0152 \left[\frac{a}{f_{rl}} \frac{(1+z)^{4-\alpha}}{\theta^3} \frac{S_i}{\nu^\alpha} \frac{\nu_2^{p+\alpha} - \nu_1^{p+\alpha}}{r(p+\alpha)} \right]^{2/7} \text{ (G)} \quad (3)$$

S_i (in mJy) is the integrated flux density of the source measured at frequency ν (in GHz) and angular size θ (in mas), α is the spectral index, z is the redshift of the source, and r is the comoving distance in Mpc. Here we take $p = 0.5$, $\alpha = \alpha_{\text{thin}}$ in the optically thin part of the spectrum from $\nu_1 \sim 1$ GHz to $\nu_2 \sim 10$ GHz, a filling factor for the relativistic plasma $f_{rl} = 1$, a relative contribution of the ions to the energy $a = 2$, and the comoving distance r in Mpc. By adopting the standard Λ CDM cosmology and using the cosmology calculator provided by NED⁵, $r = 12.7$ Mpc in this case. Here we use the

⁵ <https://www.astro.ucla.edu/~wright/CosmoCalc.html>

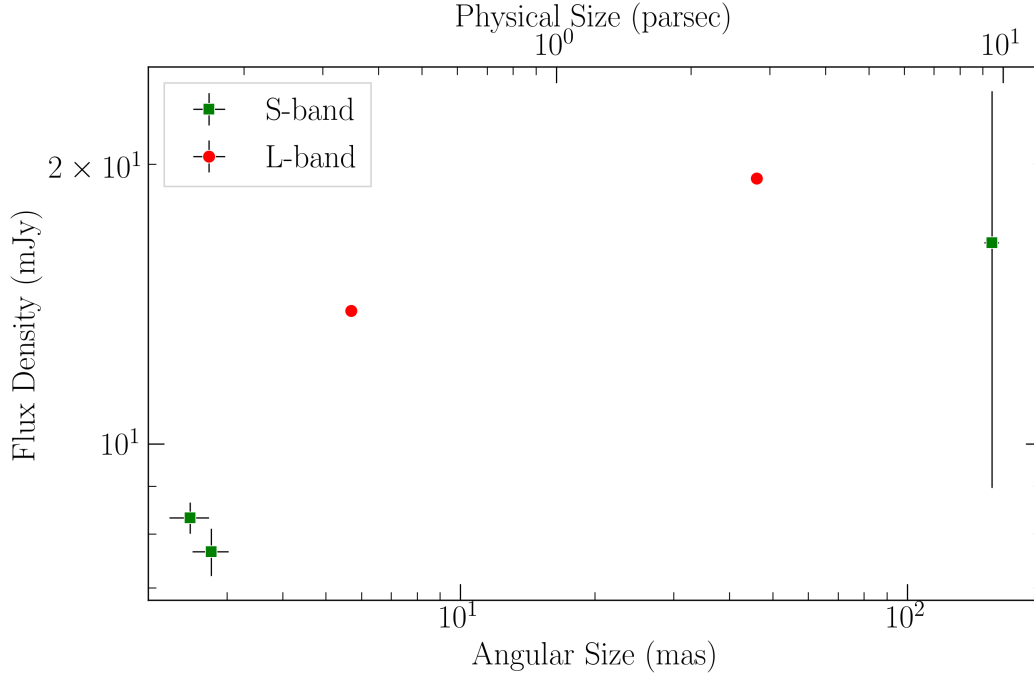


Figure 3. The radio flux density of NGC 4293 over a collection area range from ~ 2 to ~ 200 arcsec. The integrated radio flux densities and uncertainties of NGC 4293 in L (1.4) and S-band (3 GHz) are shown (Table 1). As NGC 4293 is not resolved in the given observations, the synthesised beams are taken to represent the collection area. As we use log scales, the intervals between L and S-band flux density represent the radio spectral index.

integrated flux density of 19.83 mJy estimated through formula 1 and fitting parameters, at the typical frequency of 1 GHz and angular size of 20 arcsec, which yield $B_{\min} = 3 \times 10^{-4}$ G. The magnetic field is consistent with the typical value of PS sources, e.g. gigahertz peaked-spectrum (GPS, $B \sim 10^{-3}$ G) and compact steep spectrum (CSS, $B \sim 10^{-4}$ G) radio sources (O’Dea 1998).

The electron lifetime for a turnover-type spectral radio source can be estimated as follow (O’Dea 1998)

$$t \approx 8.22 \times \frac{B^{1/2}}{B^2 + B_R^2} \times ((1+z)\nu_p)^{-1/2} \text{ (yr)} \quad (4)$$

where B is the magnetic field in G, $B_R \approx 4(1+z)^2 \times 10^{-6}$ G is the equivalent magnetic field of the microwave background, and ν_p is the break frequency in GHz. For NGC 4293, using these values estimated above, i.e. $B = 3 \times 10^{-4}$ G and $\nu_p = 0.44$ GHz, we find the electron lifetime is $\sim 1 \times 10^6$ years.

4 DISCUSSION

4.1 A peaked spectrum radio source

The brightness temperatures for components N and S are $10^{7.2}$ and $10^{6.5}$ K, respectively, favoring a non-thermal origin. Both components N and S show edge-brightening structure and inverse symmetric appearance with each other (see Figure 1). The angular distance between N and S is ~ 120 mas, corresponding to ~ 7 parsec. The whole milliarcsec-scale radio morphology of NGC 4293 resembles a compact symmetric object (CSO, O’Dea 1998; O’Dea & Saikia 2021). Along with the radio spectrum and 1.4 GHz radio power of $\sim 10^{20}$ W Hz $^{-1}$, the source belongs to a sample of (megahertz) peaked spectrum (PS/MPS) radio sources (O’Dea & Saikia 2021) (or based on the historical definition, NGC 4293 can be marginally

identified as gigahertz peaked-spectrum or compact steep-spectrum radio sources, O’Dea 1998). The PS scenario hints at an absorbed radio core in the symmetric center of the whole structure. The integrated radio spectrum of the source shows a turnover at the frequency 0.44 GHz, which is consistent with a low redshift PS source. On the other hand, the whole morphology and integrated spectrum are unlikely to be caused by a core-jet structure. Again, the core-jet scenario, where component S (inverted spectrum, see below) is the core and component N (steep spectrum, see below) is a radio lobe, will result in a discrepancy: the non-detection of a counter-jet lobe indicates that jet versus counter-jet flux ratio > 30 in this scenario, while explaining this as a beaming effect requires large advancing speed and small view angle to the jet beam. It is unlikely that the object acts this way due to the extremely low advancing speed (see below), the edge-on disk of the host and the nature that the source is not a blazar. Therefore, it again disfavors the core-jet explanation. On the origin of the spectral turnover, the rising spectral index $\alpha_{\text{thick}} = 1.29^{+0.58}_{-0.33}$ is below the critical slope $\alpha_c = +2.5$ of a free-free absorption. Thus, it favors an origin of synchrotron self-absorption mechanism, while a free-free absorption cannot be fully ruled out with the limited data (O’Dea & Saikia 2021). Blackhole mass measurements for young radio sources (including PS sources) indicate that they have a mass range from $\log(M_{\text{BH}}/M_{\odot}) \sim 7.32$ to 9.84 (Liao & Gu 2020). Therefore, whatever the different black hole mass measurements of NGC 4293, the source stands out as one of the lightest and nearest PS sources until now (e.g. Snellen et al. 2004; O’Dea & Saikia 2021).

Interestingly, the brightness of components N and S is quite asymmetric (see Figure 1), and their VLBA 1.5 GHz luminosity ratio is 3.23, hinting at an interaction with dense medium (see, e.g. Saikia et al. 2001; Thomasson et al. 2003; O’Dea & Saikia 2021). Additionally, the lobes of components N and S have lateral structures other than pointing directly away from the symmetric center (or the

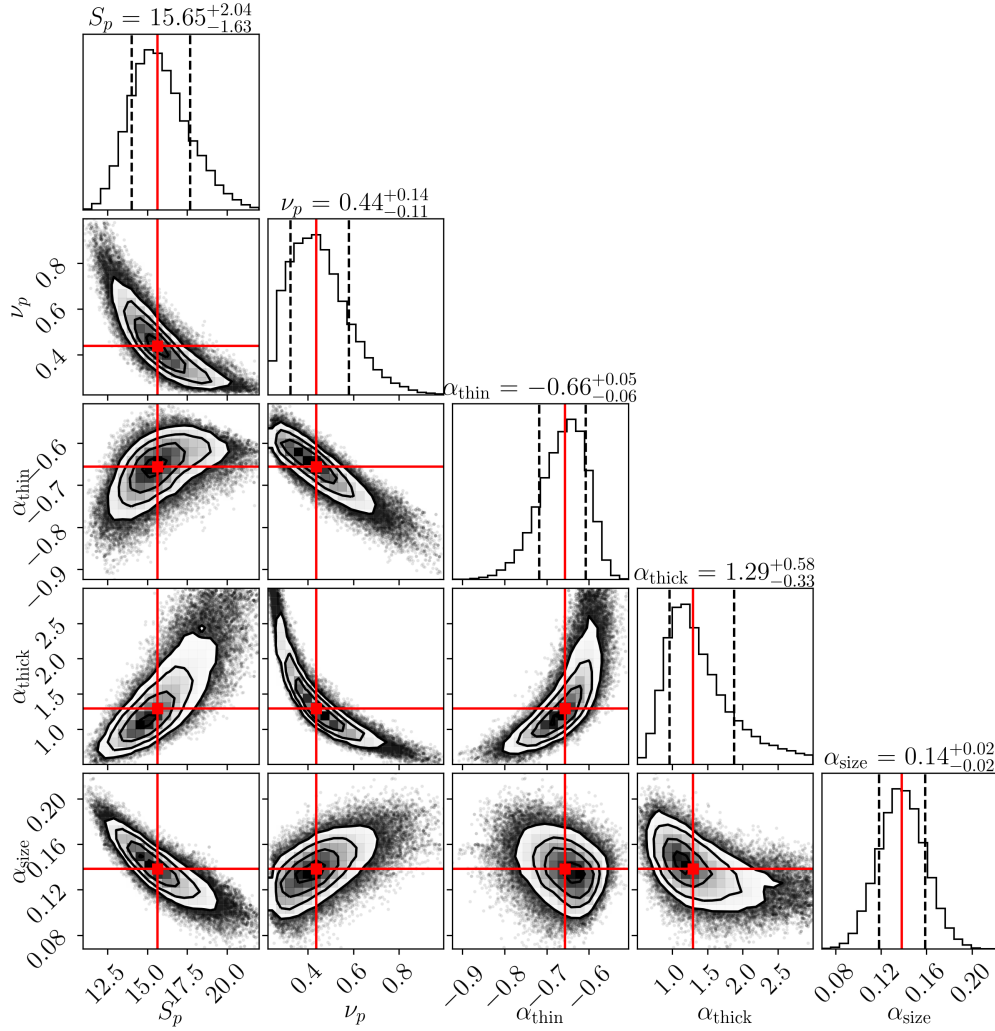


Figure 4. Marginalised and joint posterior probability distribution for the model parameters in the MCMC approach. We take 50% of the distributions as the best-fit values, which are marked in red cross-hairs and red lines. The left and right black dashed lines indicate 16% and 84% of the distributions and hence the lower and upper limit for the best-fit values, respectively

Table 1. Total radio flux density from archival observations.

Survey or Facility	Frequency (GHz)	Date	S_i (mJy)	Beam (arcsec)	References
TGSS	0.147	2016-03-15	9.50 ± 3.11	25	Intema et al. (2017)
TGSS	0.147	2010-05-27	9.67 ± 1.53	25	Intema et al. (2017)
RACS	0.887	2019-04-24	20.01 ± 0.29	15	McConnell et al. (2020)
NVSS	1.4	1993-11-15	19.3 ± 1.1	46	Condon et al. (1998)
FIRST	1.4	1999-01-15	13.90 ± 0.13	5.69 ± 0.17	White et al. (1997)
Arecibo	2.38	1975-08-01	20 ± 4	162	Dressel & Condon (1978)
VLA	3	2019-03-21	7.65 ± 0.25	2.77 ± 0.44	Lacy et al. (2020)
VLA	3	2021-11-20	8.32 ± 0.25	2.48 ± 0.32	Lacy et al. (2020)
Effelsberg	4.85	2000-2003	11 ± 3	147	Vollmer et al. (2004)
Effelsberg	8.6	2000-2003	5 ± 1	85	Vollmer et al. (2004)
Effelsberg	10.55	2000-2003	6 ± 1	69	Vollmer et al. (2004)
VLA-A [†]	4.86	2004-10-23	4.68 ± 0.10	0.58 ± 0.08	This work
VLA-A [†]	8.46	2004-10-23	2.64 ± 0.06	0.41 ± 0.05	This work

[†]: Model-fitting results of the bright and compact nuclear component.

TGSS: the TIFR GMRT Sky Survey; RACS: the Rapid ASKAP Continuum Survey; NVSS: the NRAO VLA Sky Survey; FIRST: Faint Images of the Radio Sky at Twenty-centimeters; VLA: the Very Large Array Sky Survey.

Table 2. Model-fitting results of components N and S in NGC 4293

Components	S_i (mJy)	S_p (mJy beam ⁻¹)	ϕ (mas)	$\log T_B$ (K)	$\log L_R$ (erg/s)	$\theta_{b,maj}$ (mas)	$\theta_{b,min}$ (mas)	PA ($^\circ$)
VLBA 1.5 GHz (Tapered)								
N	3.37 ± 0.18	2.70 ± 0.17	12.5	7.2	36.00 ± 0.02	33	18	44
S	1.03 ± 0.06	0.72 ± 0.05	15.0	6.5	35.48 ± 0.02	33	18	44
MERLIN 5 GHz								
N	1.58 ± 0.15	1.51 ± 0.18	6.5	6.4	36.18 ± 0.04	79	49	26
S	1.52 ± 0.15	1.08 ± 0.18	37.9	4.8	36.16 ± 0.04	79	49	26

Column 1: component name; Column 2: integrated flux density; Column 3: peak flux density; Column 4: deconvolved component size; Column 5: radio brightness temperature; Column 6: total luminosity; Column 7 - 9: beam major axis, minor axis, and position angle.

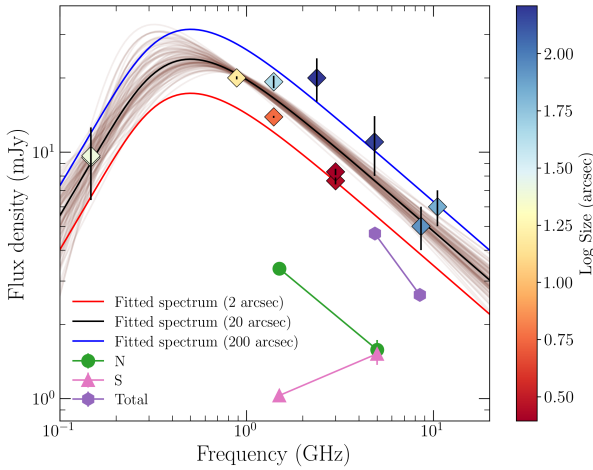


Figure 5. Radio spectrum of NGC 4293. The integrated radio flux densities are shown, where the flux densities and uncertainties are taken from Table 1. The black, blue, and red solid line is the best-fit spectrum for an angular scale of 20, 200 and 2 arcsec based on the parameters of the maximum likelihood distribution. The brown lines are from a random sampling in the Markov chain Monte Carlo approach for an angular scale of 20 arcsec and represent uncertainties of parameters. The green and pink data points are for the components N and S, respectively. The violet data points are for the central compact components in VLA A-array 4.86 and 8.46 GHz, including both components N and S.

nucleus), further suggesting the deflection of a jet due to a dense inhomogeneous and asymmetric external medium on opposite sides of the nucleus (e.g. Choi et al. 2007; O’Dea & Saikia 2021). According to the spectral age (electron lifetime) of $\sim 1 \times 10^6$ years, the source was likely frustrated by a dense medium as it results in an extremely low advancing velocity ($1.1 \times 10^{-5} c$ or 3.4 km s^{-1} , where c is the speed of light) for the lobes. Indeed, dense molecular gas was observed in NGC 4293 and concentrated in the nuclear region (Kuno et al. 2002).

The 1.5 - 5 GHz radio spectrum of component N is aligned with the integrated spectrum, while component S has a deviation from the integrated spectrum. A natural assumption is that both components are produced simultaneously, therefore having similar internal parameters. If so, the inverted spectrum at the location of component S requires an additional mechanism to further absorb the low-energy electrons – the free-free absorption by the external ionized dense gas is possibly at work for the southern component. The exactly differ-

ent spectral indices for the jet and the counter-jet lobes are common in radio sources (e.g. Walker et al. 2000; Sokolovsky et al. 2011) and one of the promising explanations is the free-free absorption by circumnuclear medium (e.g. Walker et al. 2000). Again the hypothesis is supported by the Wide-field Infrared Survey Explorer (WISE) emission near the position of component S. The ALLWISE program obtained 1σ astrometric accuracy of 0.033 arcsec (Cutri et al. 2021) (see error-bars in panel c of Figure 2), therefore, it is still close to component S by taking 3σ positional uncertainty of ~ 0.1 arcsec and clearly differs from component N. *Gaia* Early Data Release 3 (EDR3) measured the optical core of NGC 4293 and obtained 3σ astrometric uncertainty of ~ 0.01 arcsec (Gaia Collaboration et al. 2016, 2021), which is close to component N. Because the host galaxy is edge-on, the optical position naturally offsets towards the north direction (see panels a and b of Figure 2) due to the obstruction of the dust lane.

4.2 On the black hole mass and accretion

In measuring black hole mass, both the stellar velocity and the K_S -band bulge luminosity-based methods have intrinsic dispersion of at least 1 dex (Kormendy & Ho 2013), which is even worse in the low-mass end. On the other hand, LINERs have very different accretion flow (Ho et al. 2003; Ho 2008, 2009) and broad emission line regions (e.g. Ho et al. 1997b). Therefore, estimating black hole mass from the single-epoch broad H α emission for the LINER NGC 4293 (Chilingarian et al. 2018) may induce a large uncertainty. Again, LINERs tend to have extremely low accretion rates (Ho et al. 2003; Ho 2008, 2009), while the unreasonably high Eddington ratio $\lambda_{\text{Edd}} = 0.25$ (> 0.01) (Chilingarian et al. 2018) would further hint at an underestimation of black hole mass in Chilingarian et al. (2018). It is essential to constrain the black hole mass of NGC 4293 with a radio-based method, e.g. the fundamental plane of black hole activity (Merloni et al. 2003).

The fundamental plane relation among nuclear radio luminosity, nuclear X-ray luminosity, and black hole mass unified the accretion and ejection process in compact systems. The existence of such a relationship is based on that the radio emission is produced in a jet/outflow, and X-ray emission is produced in a disk-corona system. Both radio and X-ray power are related to black hole mass and accretion rate. Therefore, the fundamental plane relation is thought to work in any accretion system which is in a quiescent or low/hard accretion state (associated with a steady ejection, see Gallo et al. 2003; Merloni et al. 2003). Additionally, the very high/intermediate state may also

produce radio ejection that can follow the same trend (see Merloni et al. 2003, they also include transient sources). However, including sources in a very high/intermediate state induces a dispersion in the fundamental plane relation. This is primarily due to the evolution of individual radio blobs, as the radio ejecting process is episodic in this state. There are several works exploring the fundamental plane relation on CSOs (morphological candidates of PS sources, Fan & Bai 2016; Wójtowicz et al. 2020; Liao et al. 2020). Most of the results suggest CSOs do deviate from the classical trends. Two types of known contamination are (1) radio emissions from lobes will be enhanced when they propagate through a dense medium (O’Dea & Saikia 2021); (2) X-ray emission contains a contribution from the jet, e.g., through synchrotron or inverse Compton mechanisms (Stawarz et al. 2008). Furthermore, the radio emissions from lobes of CSOs are not associated with the X-ray emission collected in the core region, because the radio emissions from lobes are substantially produced in different epochs from the core X-ray emission, e.g. $\sim 1 \times 10^6$ years ago in NGC 4293.

NGC 4293 have Eddington ratio $\lambda_{\text{Edd}} = 0.001 - 0.25$, corresponding to the black hole masses range from $10^{7.7}$ to $10^{5.3} M_{\odot}$. The Eddington ratio $\lambda_{\text{Edd}} \equiv L_{\text{bol}}/L_{\text{Edd}}$, where $L_{\text{bol}} = 10L_{\text{B}}$ and $L_{\text{Edd}} = 1.26 \times 10^{38} (M_{\text{BH}}/M_{\odot})$ (erg/s) (see also Yang et al. 2020b). The calculation above takes $10L_{\text{B}}$ as the bolometric luminosity, where $L_{\text{B}} = 41.8 \text{ erg s}^{-1}$ is *B*-band luminosity of NGC 4293. Here the *B*-band luminosity is estimated from $H\alpha$ line luminosity of NGC 4293 (Chilingarian et al. 2018) through the method described in (e.g. Greene & Ho 2007; Dong et al. 2012; Chilingarian et al. 2018). The critical Eddington ratio from low to high-state is $\lambda_{\text{Edd}} = 0.01$ (Gallo et al. 2003). Furthermore, a recent work (Yang et al. In preparation) studies a sample of IMBHs with VLBA, and it indicates that parsec-scale radio emissions from IMBHs can follow Merloni et al. (2003)’s fundamental plane very well. In order to keep the simultaneity between radio and X-ray observations, here we firstly estimate the black hole mass of NGC 4293 by taking the radio emission from the core region. If we take a $3\sigma = 0.3 \text{ mJy}$ upper limit in the MERLIN image as the core radio flux density, then the 5 GHz core radio luminosity is $\log L_{\text{core}, 5\text{GHz}} = 35.46 \text{ erg s}^{-1}$ (redshift effect can be negligible). Here we take the X-ray luminosity from the *Chandra* observation and assume that $\log L_{\text{X}(2-10\text{keV})} \simeq \log L_{\text{X}(0.5-8\text{keV})} = 39.69 \text{ erg s}^{-1}$ (Soria et al. 2022). Additionally, an observation with *ROSAT* gives $\log L_{\text{X}(0.1-2.4\text{keV})} = 39.48 \text{ erg s}^{-1}$ (Halderson et al. 2001). The resulting black hole mass of NGC 4293 is $\log (M_{\text{BH}}/M_{\odot}) = 5.53$, consistent with the latest measurement by Chilingarian et al. (2018). An exploration of fundamental plane relation on a sample of CSOs (with radio flux density from lobes) indicates that they can follow the trend, while their radio luminosity is ~ 1 dex higher than the original fitting of the fundamental plane relation (see Wójtowicz et al. 2020). If we consider the 1 dex deviation and use the radio luminosities of lobes, a similar black hole mass $\log (M_{\text{BH}}/M_{\odot}) \sim 5.16$ can be estimated. As most of CSOs have a radio-quiet core (O’Dea & Saikia 2021), the use of the lobe’s radio luminosity in the fundamental plane should be explored further. We also used the method described here to measure the black hole mass of another IMBH candidate RGG 9 (Reines et al. 2013). Using the radio luminosity presented by Yang et al. (2020a), our black hole mass estimate matches very well with the measurement by using virial techniques (Reines et al. 2013).

We have to bear in mind that Merloni et al. (2003)’s fundamental plane of black hole activity has a large dispersion. Taking the upper limit of the 5 GHz core radio luminosity, we estimate black hole mass using Saikia et al. (2018) correlation as $\log (M_{\text{BH}}/M_{\odot}) = 5.9 \pm 2.0$. Again, using the most recent version of the fundamental plane of BH activity (Gültekin et al. 2019), we obtain $\log (M_{\text{BH}}/M_{\odot}) = 5.9 \pm$

0.3. Alternatively, directly using the 1 dex reduced radio luminosity of lobes and Gültekin et al. (2019) correlation, we roughly obtain $\log (M_{\text{BH}}/M_{\odot}) = 5.6 \pm 0.3$. Furthermore, we note that the X-ray luminosity of NGC 4293 is under-estimated due to the absorption of the circumnuclear medium in the host galaxy (Halderson et al. 2001; Soria et al. 2022), therefore resulting in an over-estimating of black hole mass through the fundamental plane of black hole activity. In summary, the fundamental plane of black hole activity would refine the black hole mass of NGC 4293 to be $\lesssim 10^6 M_{\odot}$. Therefore, the object is a low-mass AGN and a potential candidate for IMBHs as well.

In X-ray binaries, an episodic ejection is produced when the accretion is in a very high/intermediate state (Fender et al. 2004). Interestingly, an episodic ejection is already observed in the IMBH candidate HLX-1 when it is in a high X-ray state (Webb et al. 2012). In the unification model of accretion process (McHardy et al. 2006), AGNs should also have specific accretion states and relevant state transitions as that are universally observed in Galactic XRBs (Fender et al. 2004). Naturally, multi-types of accretion state should also be expected in IMBHs, and according to the scaling relation, it should play much faster than it is in AGNs (as the timescale is proportional to black hole masses, e.g. Svoboda et al. 2017). Here, the spectral age of the radio emission in NGC 4293, $\sim 1 \times 10^6$ years, is slightly larger than an episodic activity of the radiation pressure instabilities in accretion disks (i.e. $10^4 - 10^5$ year, O’Dea & Saikia 2021). If so, future high-resolution observations of IMBHs at low frequencies ($< 1 \text{ GHz}$) will help to reveal radio emissions or bubbles from the relic of ejecta. Monitoring observations may also help in capturing the episodic ejection directly and revealing the evolution of radio blobs.

5 CONCLUSION

In summary, we performed a Very Long Baseline Array (VLBA) L-band (1.5 GHz) observation of the IMBH candidate in the nucleus of the LINER galaxy NGC 4293 ($z = 0.003$). By cooperating with the archive VLA and MERLIN data, we find (1) the source has two radio blobs with a projected distance of ~ 7 parsec apart from each other and its integrated spectrum has a turnover at $\sim 0.44 \text{ GHz}$. Therefore it can be allocated as a typical compact symmetric object (CSO). We also find evidence that the lobes are interacting with the dense medium. Despite different mass estimations, the source stands out as one of the lightest and nearest CSOs; (2) We estimate the black hole mass of NGC 4293 through the fundamental plane of black hole activity and constrain it to be $\lesssim 10^6 M_{\odot}$. The result supports that NGC 4293 has a less massive AGN; (3) The discovery of compact symmetric ejecta in the less massive (or intermediate-mass) AGN, NGC 4293, can be reasonably explained as the source is maintaining an episodic ejection.

ACKNOWLEDGEMENTS

X.-L.Y. designed the VLBA observations, made the VLBI data reduction and model-fitting, and interpret the results, R.-L.W. contribute to drafting the manuscript, interpret the results and proof correction, and Q.G. provided useful comments on the manuscript. This work is supported by the Shanghai Sailing Program (21YF1455300) and China Postdoctoral Science Foundation (2021M693267). XLY thanks for the support from the National Science Foundation of China (12103076). We thank Luis C. Ho from the Kavli Institute

for Astronomy and Astrophysics at Peking University (KIAA-PKU), he shared important experiences and matters that need attention in measuring black hole masses of LINER galaxies. The National Radio Astronomy Observatory is a facility of the National Science Foundation operated under cooperative agreement by Associated Universities, Inc. *e*-MERLIN is a National Facility operated by the University of Manchester at Jodrell Bank Observatory on behalf of STFC. This work has made use of data from the Pan-STARRS1 Surveys (PS1) and the PS1 public science archive. This work has made use of data from the European Space Agency (ESA) mission *Gaia* (<https://www.cosmos.esa.int/gaia>), processed by the *Gaia* Data Processing and Analysis Consortium (DPAC, <https://www.cosmos.esa.int/web/gaia/dpac/consortium>).

DATA AVAILABILITY

Scientific results from data presented in this publication are derived from the VLBA project BA146. The correlated data are available in the NRAO Science Data Archive (<https://data.nrao.edu>).

REFERENCES

- Bañados E., et al., 2018, *Nature*, **553**, 473
 Callingham J. R., et al., 2017, *ApJ*, **836**, 174
 Chiaberge M., Capetti A., Macchetto F. D., 2005, *ApJ*, **625**, 716
 Chilingarian I. V., Katkov I. Y., Zolotukhin I. Y., Grishin K. A., Beletsky Y., Boutsia K., Osip D. J., 2018, *ApJ*, **863**, 1
 Choi E., Wiita P. J., Ryu D., 2007, *ApJ*, **655**, 769
 Condon J. J., Cotton W. D., Greisen E. W., Yin Q. F., Perley R. A., Taylor G. B., Broderick J. J., 1998, *AJ*, **115**, 1693
 Cutri R. M., et al., 2021, *VizieR Online Data Catalog*, **p. II/328**
 Decarli R., Gavazzi G., Arosio I., Cortese L., Boselli A., Bonfanti C., Colpi M., 2007, *MNRAS*, **381**, 136
 Dong X. Y., De Robertis M. M., 2006, *AJ*, **131**, 1236
 Dong X.-B., Ho L. C., Yuan W., Wang T.-G., Fan X., Zhou H., Jiang N., 2012, *ApJ*, **755**, 167
 Dressel L. L., Condon J. J., 1978, *ApJS*, **36**, 53
 Fan X.-L., Bai J.-M., 2016, *ApJ*, **818**, 185
 Faucher-Giguère C.-A., Quataert E., 2012, *MNRAS*, **425**, 605
 Fender R. P., Belloni T. M., Gallo E., 2004, *MNRAS*, **355**, 1105
 Filho M. E., Barthel P. D., Ho L. C., 2006, *A&A*, **451**, 71
 Fomalont E. B., 1999, in Taylor G. B., Carilli C. L., Perley R. A., eds, *Astronomical Society of the Pacific Conference Series Vol. 180, Synthesis Imaging in Radio Astronomy II*. p. 301
 Gaia Collaboration et al., 2016, *A&A*, **595**, A1
 Gaia Collaboration et al., 2021, *A&A*, **649**, A1
 Gallo E., Fender R. P., Pooley G. G., 2003, *MNRAS*, **344**, 60
 Greene J. E., 2012, *Nature Communications*, **3**, 1304
 Greene J. E., Ho L. C., 2004, *ApJ*, **610**, 722
 Greene J. E., Ho L. C., 2007, *ApJ*, **670**, 92
 Greene J. E., Ho L. C., Ulvestad J. S., 2006, *ApJ*, **636**, 56
 Greene J. E., Strader J., Ho L. C., 2020, *ARA&A*, **58**, 257
 Greisen E. W., 2003, *AIPS*, the VLA, and the VLBA. p. 109
 Gültekin K., King A. L., Cackett E. M., Nyland K., Miller J. M., Di Matteo T., Markoff S., Rupen M. P., 2019, *ApJ*, **871**, 80
 Halderson E. L., Moran E. C., Filippenko A. V., Ho L. C., 2001, *AJ*, **122**, 637
 Ho L. C., 2008, *ARA&A*, **46**, 475
 Ho L. C., 2009, *ApJ*, **699**, 626
 Ho L. C., Filippenko A. V., Sargent W. L. W., 1997a, *ApJS*, **112**, 315
 Ho L. C., Filippenko A. V., Sargent W. L. W., Peng C. Y., 1997b, *ApJS*, **112**, 391
 Ho L. C., Filippenko A. V., Sargent W. L. W., 2003, *ApJ*, **583**, 159
 Hwang H.-C., Zakamska N. L., Alexandroff R. M., Hamann F., Greene J. E., Perrotta S., Richards G. T., 2018, *MNRAS*, **477**, 830
 Inayoshi K., Visbal E., Haiman Z., 2020, *ARA&A*, **58**, 27
 Intema H. T., Jagannathan P., Mooley K. P., Frail D. A., 2017, *A&A*, **598**, A78
 King A., Pounds K., 2015, *ARA&A*, **53**, 115
 Kormendy J., Ho L. C., 2013, *ARA&A*, **51**, 511
 Kuno N., Nakai N., Sorai K., Nishiyama K., Vila-Vilaó B., 2002, *PASJ*, **54**, 555
 Lacy M., et al., 2020, *PASP*, **132**, 035001
 Liao M., Gu M., 2020, *MNRAS*, **491**, 92
 Liao M., Gu M., Zhou M., Chen L., 2020, *MNRAS*, **497**, 482
 Liu H.-Y., Yuan W., Dong X.-B., Zhou H., Liu W.-J., 2018, *ApJS*, **235**, 40
 McClintock J. E., Remillard R. A., 2006, in , Vol. 39, *Compact stellar X-ray sources*. pp 157–213
 McConnell D., et al., 2020, *Publ. Astron. Soc. Australia*, **37**, e048
 McHardy I. M., Koerding E., Knigge C., Uttley P., Fender R. P., 2006, *Nature*, **444**, 730
 Merloni A., Heinz S., di Matteo T., 2003, *MNRAS*, **345**, 1057
 Mezcuca M., Civano F., Marchesi S., Suh H., Fabbiano G., Volonteri M., 2018, *MNRAS*, **478**, 2576
 Mirabel F., 2017, *New Astron. Rev.*, **78**, 1
 Nagar N. M., Falcke H., Wilson A. S., Ulvestad J. S., 2002, *A&A*, **392**, 53
 Nagar N. M., Falcke H., Wilson A. S., 2005, *A&A*, **435**, 521
 Nyland K., et al., 2017, *MNRAS*, **464**, 1029
 O’Dea C. P., 1998, *PASP*, **110**, 493
 O’Dea C. P., Saikia D. J., 2021, *A&ARv*, **29**, 3
 Paragi Z., Frey S., Kaaret P., Cseh D., Overzier R., Kharb P., 2014, *ApJ*, **791**, 2
 Patil P., et al., 2022, *ApJ*, **934**, 26
 Reines A. E., Deller A. T., 2012, *ApJ*, **750**, L24
 Reines A. E., Greene J. E., Geha M., 2013, *ApJ*, **775**, 116
 Saikia D. J., Jeyakumar S., Salter C. J., Thomasson P., Spencer R. E., Mantovani F., 2001, *MNRAS*, **321**, 37
 Saikia P., Körding E., Coppejans D. L., Falcke H., Williams D., Baldi R. D., McHardy I., Beswick R., 2018, *A&A*, **616**, A152
 Shepherd M. C., 1997, in Hunt G., Payne H., eds, *Astronomical Society of the Pacific Conference Series Vol. 125, Astronomical Data Analysis Software and Systems VI*. p. 77
 Snellen I. A. G., Mack K. H., Schilizzi R. T., Tschager W., 2004, *MNRAS*, **348**, 227
 Sokolovsky K. V., Kovalev Y. Y., Pushkarev A. B., Mimica P., Perucho M., 2011, *A&A*, **535**, A24
 Soria R., et al., 2022, *MNRAS*, **512**, 3284
 Stawarz L., Ostorero L., Begelman M. C., Moderski R., Kataoka J., Wagner S., 2008, *ApJ*, **680**, 911
 Svoboda J., Guainazzi M., Merloni A., 2017, *A&A*, **603**, A127
 Thomasson P., Saikia D. J., Muxlow T. W. B., 2003, *MNRAS*, **341**, 91
 Ulvestad J. S., Antonucci R. R. J., Barvainis R., 2005, *ApJ*, **621**, 123
 Vollmer B., Thierbach M., Wielebinski R., 2004, *A&A*, **418**, 1
 Volonteri M., 2010, *A&ARv*, **18**, 279
 Walker R. C., Dhawan V., Romney J. D., Kellermann K. I., Vermeulen R. C., 2000, *ApJ*, **530**, 233
 Webb N., et al., 2012, *Science*, **337**, 554
 White R. L., Becker R. H., Helfand D. J., Gregg M. D., 1997, *ApJ*, **475**, 479
 Wójtowicz A., Stawarz L., Cheung C. C., Ostorero L., Kosmaczewski E., Siemiginowska A., 2020, *ApJ*, **892**, 116
 Wrobel J. M., Ho L. C., 2006, *ApJ*, **646**, L95
 Wu X.-B., et al., 2015, *Nature*, **518**, 512
 Yang J., Gurvits L. I., Paragi Z., Frey S., Conway J. E., Liu X., Cui L., 2020a, *MNRAS*, **495**, L71
 Yang X., et al., 2020b, *ApJ*, **904**, 200
 Yang J., Paragi Z., Nardini E., Baan W. A., Fan L., Mohan P., Varenus E., An T., 2021, *MNRAS*, **500**, 2620
 Yang J., et al., 2022, *MNRAS*, **514**, 6215

This paper has been typeset from a \LaTeX file prepared by the author.